Transport and inhibition of the sphingosine-1-phosphate exporter SPNS2

David Sauer

david.sauer@cmd.ox.ac.uk

University of Oxford   https://orcid.org/0000-0001-9291-4640

Huanyu Li

University of Oxford

Ashley Pike

University of Oxford   https://orcid.org/0000-0001-9661-2607

Yung-Ning Chang

Nuvisan

Dheeraj Prakaash

University of Oxford

Zuzana Gelova

CeMM Research Center for Molecular Medicine of the Austrian Academy of Sciences

Josefina Stanka

Bayer

Christophe Moreau

University of Oxford

Hannah Scott

University of Oxford

Frank Wunder

Bayer

Gernot Wolf

CeMM Research Center for Molecular Medicine of the Austrian Academy of Sciences

Andreea Scacioc

University of Oxford

Gavin McKinley

University of Oxford

Helena Batoulis

Bayer

Shubhashish Mukhopadhyay

University of Oxford

Andrea Garofoli

CeMM Research Center for Molecular Medicine of the Austrian Academy of Sciences

Adan Pinto-Fernandez

TDI Mass Spectrometry Laboratory, Target Discovery Institute, Nuffield Department of Medicine, University of Oxford, Oxford, Roosevelt Drive, Oxford OX3 7FZ, UK

Benedikt Kessler

University of Oxford   https://orcid.org/0000-0002-8160-2446

Nicola Burgess-Brown

University of Oxford

Saša Štefanic

University of Zurich   https://orcid.org/0000-0001-7367-1831

Tabea Wiedmer

CeMM Research Center for Molecular Medicine of the Austrian Academy of Sciences

Katharina Dürr

University of Oxford

Vera Puetter

Bayer AG

Alexander Ehrmann

Bayer

Syma Khalid

University of Southampton   https://orcid.org/0000-0002-3694-5044

Alvaro Ingles-Prieto

CeMM Research Center for Molecular Medicine of the Austrian Academy of Sciences

Giulio Superti-Furga

CeMM Research Center for Molecular Medicine of the Austrian Academy of Sciences
https://orcid.org/0000-0002-0570-1768

Article

Additional Declarations: There is **NO** Competing Interest.

1 **Transport and inhibition of the sphingosine-1-phosphate exporter SPNS2**

2

3 Huanyu Z. Li [1], Ashley C.W. Pike [1*], Yung-Ning Chang [2*], Dheeraj Prakaash [3*],

4 Zuzana Gelova [4*], Josefina Stanka [5*], Christophe Moreau [1], Hannah C. Scott [1,6], Frank

5 Wunder [5], Gernot Wolf [4], Andreea Scacioc [1], Gavin McKinley [1], Helena Batoulis [5],

6 Shubhashish Mukhopadhyay [1], Andrea Garofoli [4], Adán Pinto-Fernández [1,6], Benedikt

7 M. Kessler [1,6], Nicola A. Burgess-Brown [1], Saša Štefanić [7], Tabea Wiedmer [4],

8 Katharina L. Dürr [1†], Vera Puetter [2†], Alexander Ehrmann [5†], Syma Khalid [3†], Alvaro

9 Ingles-Prieto [4†], Giulio Superti-Furga [4,8†], David B. Sauer [1†]

10

11 1 Centre for Medicines Discovery, Nuffield Department of Medicine, University of

12 Oxford, Oxford, UK

13 2 Nuvisan ICB GmbH, Berlin, Germany

14 3 Department of Biochemistry, University of Oxford, Oxford, UK

15 4 CeMM Research Center for Molecular Medicine of the Austrian Academy of

16 Sciences, Vienna, Austria

17 5 Bayer AG

18 6 Chinese Academy for Medical Sciences Oxford Institute, Nuffield Department of

19 Medicine, University of Oxford, Oxford, UK

20 7 Nanobody Service Facility, University of Zurich, AgroVet-Strickhof, Eschikon,

21 Switzerland

22 8 Center for Physiology and Pharmacology, Medical University of Vienna, Vienna,
23 Austria

24

25

26 [*] Authors contributed equally: A.C.W.P., Y.N.C., D.P., Z.G., J.S.

27

28 [†] Correspondence to: K.D. (katharina.duerr@omass.com), V.P.

29 (Vera.Puetter@nuvisan.com), A.E. (alexander.ehrmann@bayer.com), S.K.

30 (syma.khalid@bioch.ox.ac.uk), A.I.P. (AInglesprieto@cemm.oeaw.ac.at), G.S.F.

31 (GSuperti@cemm.oeaw.ac.at), D.B.S. (david.sauer@cmd.ox.ac.uk)

32 **Abstract**

33 Sphingosine-1-phosphate (S1P) is a signaling lysolipid critical to heart development,

34 immunity, and hearing. Accordingly, mutations in the S1P transporter SPNS2 are

35 associated with reduced white cell count and hearing defects. SPNS2 also exports the

36 S1P-mimicking FTY720-P (Fingolimod) and thereby is central to the pharmacokinetics

37 of this drug when treating multiple sclerosis. Here, we use a combination of cryo-

38 electron microscopy, immunofluorescence, *in vitro* binding and *in vivo* S1P export

39 assays, and molecular dynamic simulations to probe SPNS2's substrate binding and

40 transport. These results reveal the transporter's binding mode to its native substrate

41 S1P, the therapeutic FTY720-P, and the SPNS2-targeting inhibitor 33p. Further

42 capturing an inward-facing apo state, our structures illuminate the protein's

43 mechanism for exchange between inward-facing and outward-facing conformations.

44 Finally, using these structural, localization, and S1P transport results, we identify how

45 pathogenic mutations ablate the protein's export activity and thereby lead to hearing

46 loss.

47

48 **Introduction**

49 Sphingosine-1-phosphate (S1P) is a bioactive lipid central to cell growth, embryonic

50 development, and the physiology and pathophysiology in multiple tissues. S1P is

51 essential to vascular and cardiac development [1,2], and maintenance of the blood-brain

52 barrier [3]. The S1P concentration gradient in peripheral lymphoid organs is critical for

53 the migration of lymphocytes [4]. Accordingly, the S1P signaling pathway is targeted by

54 several clinically approved or evaluated therapeutics for auto-immune diseases

55 including multiple sclerosis and ulcerative colitis [5,6]. Finally, while its role is complex,

56 the lipid is central to cancer by regulating vascularization, inflammation, and cell

57 growth [7].

58

59 Sphingosine-1-phosphate is generated from sphingosine in the cytoplasm by the

60 sphingosine kinases [8]. The signaling lipid is subsequently exported to the extracellular

61 space by several plasma membrane export proteins, including Spinster Homolog 2

62 (SPNS2), MFSD2B, ABCA1, ABCA7, ABCC1, and ABCG2 [9]. Of these, SPNS2 is the

63 primary exporter of S1P into lymph [10]. Accordingly, knock-out of SPNS2 in mice

64 prevents immune cell egress into lymph and blood [10], and a single nucleotide variant

65 is associated with white cell count in humans [11]. Additionally, loss of SPNS2 function

66 leads to hearing defects in humans and mice due to disorganization of the stria

67 vascularis and loss of the endocochlear potential [12,13].

68

69 Notably, SPNS2 also plays a central role in the therapeutic targeting of sphingosine-

70 1-phosphate signaling. The S1P receptor (S1PR) antagonist fingolimod is

71 administered as the prodrug FTY720 and phosphorylated intracellularly into the

72 bioactive FTY720 phosphate (FTY720-P) [14]. Exported by SPNS2, FTY720-P

73 subsequently induces internalization and downregulation of S1P receptors [15],

74 ultimately leading to lymphopenia [16]. However, the S1PR antagonists have

75 cardiovascular side effects due to receptor expression in cardiac cells [17]. Therefore,

76 alternative methods of targeting S1P signaling are of significant interest [18], and SPNS2

77 itself has been the target for small-molecule inhibitor development [19,20].

78

79 Historically, understanding of SPNS2's binding to substrates and inhibitors has been

80 limited by a lack of structural data for the transporter, challenging structure-based drug

81 design. Several distantly related transporters from the larger major facilitator

82 superfamily serve as prototypes for MFS lipid transport [21,22], including the

83 lysophospholipid importer MFSD2A [23–26] and the orphan transporter HnSPNS from

84 *Hyphomonas neptunium* [27]. Recently, apo structures of human SPNS2 in an outward-

85 facing conformation (C_o-apo), and inward-facing structures in complex with S1P (C_i-

86 S1P) and the inhibitor 16d (C_i-16d), have shed light on the protein's transport and

87 inhibition [28]. However, the mechanism of substrate entry to the binding site, and the

88 outward-to-inward conformational change, remain ambiguous without an inward-

89 facing apo state. Further, positioning of the S1P head group in the substrate-bound

90 SPNS2 structure would preclude a classic MFS rocker-switch mechanism [29],

91 necessitating further investigation of substrate binding and transport. Finally, the

92 transporter's interactions with FTY720-P and the high-affinity SPNS2 inhibitor

93 SLB1122168 (33p) remain undescribed.

94

95   To address these gaps in our knowledge of SPNS2 transport and enable therapeutic

96   targeting of the transporter, we determined cryo-electron microscopy (cryo-EM) of

97   inward-facing SPNS2 in an apo state and bound to a substrate surrogate. In

98   conjunction with these structural results, we used molecular dynamics simulations and

99   a biochemical thermostability assay to characterize the transporter's interactions with

100   S1P, FTY720-P, and a SPNS2-targeting inhibitor. Finally, we report a S1PR3-coupled

101   S1P transport assay amenable for high-throuput screening of SPNS2 activity.

102   Together, these provide valuable insights into SPNS2's transport activity and enable

103   its therapeutic targeting.

104

105   **Results**

106   **Anti-SPNS2 nanobody generation and subcellular localization**

107   To enable nanobody generation, biophysical, and structural studies of SPNS2, we first

108   over-expressed the protein in HEK293 cells using the BacMam system and purified

109   the protein to homogeneity in n-dodecyl-β-D-maltopyranoside (DDM) or lauryl maltose

110   neopentyl glycol (LMNG) (Supplementary Fig. 1a-c). The solubilized SPNS2 was

111   thermostabilized by FTY720-P in a dose-dependent manner up to 2 °C (Fig. 1a,

112   Supplementary Fig. 1d). However, FTY720-P did not stabilize another major facilitator

113   transporter, the voltage-gated purine nucleotide uniporter (VNUP) (Supplementary

114   Fig. 1e). This indicates that solubilized and purified SPNS2 is properly folded and

115   capable of binding substrate through specific interactions with the transporter.

116

117   Immunizing alpacas with SPNS2, we identified nanobodies D12 (NbD12) and F09

118   (NbF09) which bind SPNS2 with affinities of 7.75 nM and 368 nM, respectively (Fig.

119   1b, Supplementary Fig. 1f). To further validate the nanobodies in cells, and test their

120   applicability for *in vivo* studies, we took advantage of a HEK293 cell line with inducible

121   overexpression of SPNS2 fused to an HA tag. With negative and positive controls of

122   cells without induction or induced cells, we found that SPNS2 localizes to the plasma

123   membrane and both NbD12 and NbF09 co-localize with the transporter (Fig. 1c,

124   Supplementary Fig. 1g). Confirming their ability to bind solubilized SPNS2, co-

125   immunoprecipitation with the nanobodies from cells pulled down the transporter from

126   expressing cells (Supplementary Fig. 1h). These results confirm that NbD12 and

127 NbF09 are highly specific for SPNS2 and bind the transporter in detergent and its
128 native membrane.
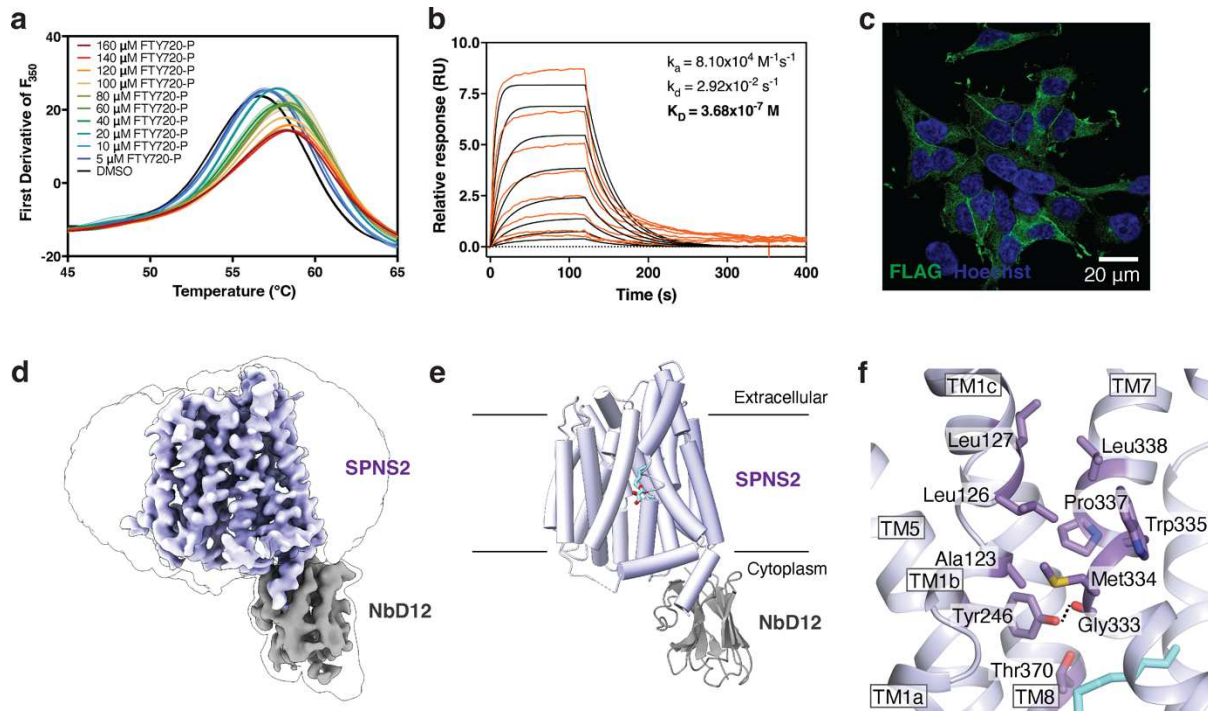
Figure 1. Structure of detergent-solubilized SPNS2. a. Measurement of LMNG-
purified SPNS2 by FTY720-P using nano-Differential Scanning Fluorescence (N = 3).
Data are presented as mean ± SEM. **b**. Binding affinity and kinetics of NbF09 as
determined by Bio-layer Interferometry. Injections at various concentrations and best
fits are shown as orange and black lines, respectively. **c**. Anti-FLAG
immunofluorescence of SPNS2 overexpressing cells stained with FLAG-tagged
NbF09 and Hoechst dye. **d**. Cryo-EM map of the SPNS2-NbD12 complex determined
in DDM. Transporter and nanobody are colored in purple and grey, respectively. The
detergent micelle and extent of the entire molecule are shown by a thin black outline
(blurred version of the same cryo-EM map). **e**. Structure of the SPNS2-NbD12
complex determined in DDM viewed from the plane of the membrane. **f**. Residues
sealing the extracellular gate of SPNS2. Hydrogen bonds are shown as dotted lines.

Inward-facing structure of SPNS2

We next set out to determine an experimental structure of full-length SPNS2 to
examine its binding and transport of S1P. However, the small size of SPNS2
presented a challenge for single-particle cryo-EM. As NbD12 bound SPNS2 with
higher affinity than NbF09, we prepared and purified the SPNS2-NbD12 complex
(Supplementary Fig. 3a, b) and determined its structure by cryo-EM (Fig. 1d,
Supplementary Fig. 3c, Supplementary Table 1). This 3.7 Å resolution map of the
SPNS2-NbD12 complex in DDM (SPNS2-DDM) was sufficient to build and refine the

151   entire transporter except for the highly mobile N-terminus, extramembrane loops L6-
152   7, and L7-8 (Fig. 1e).
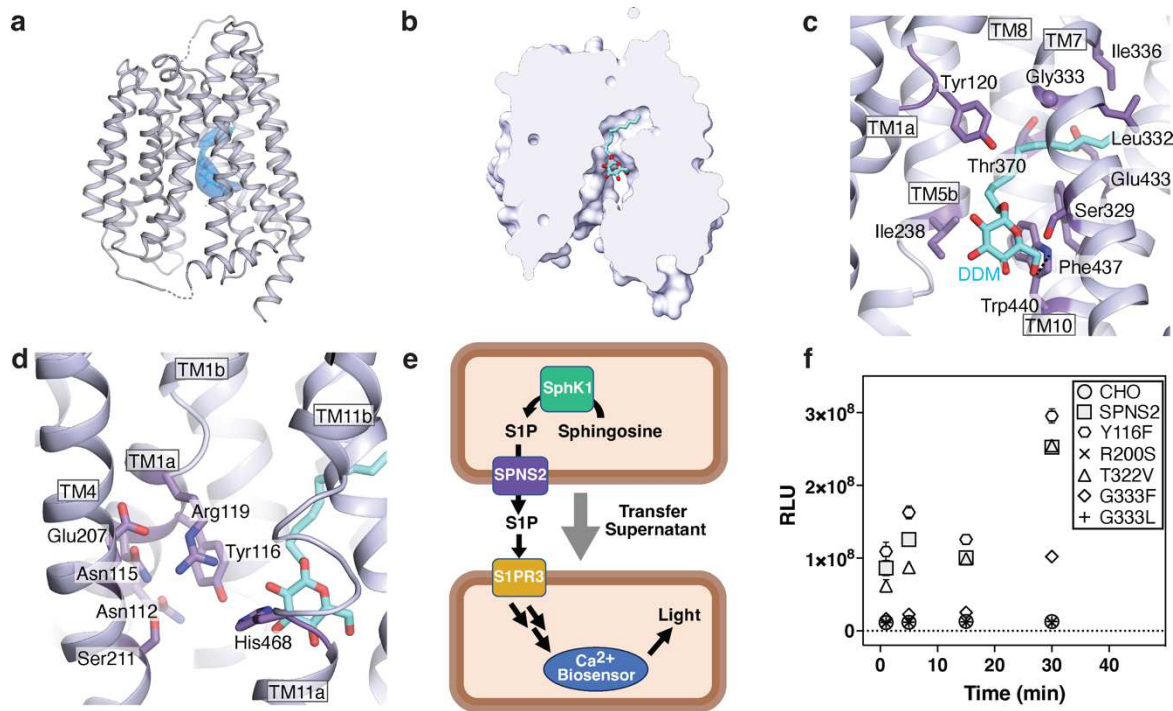
154   **Figure 2. DDM binding pocket of SPNS2. a.** Bound n-dodecyl-β-D-maltopyranoside
155   within the SPNS2 structure determined in DDM. Positive difference density of the
156   weighted F_o–F_c difference map at 16σ and the DDM model are shown as blue surface
157   and DDM cyan sticks, respectively. **b**. Cross section of the SPNS2 structure, viewed
158   from the plane of the membrane. **c**. SPNS2 coordinates DDM through van der Waals
159   contacts in the pocket and hydrogen bonds in the central cavity. SPNS2-DDM
160   hydrogen bonds are shown as dotted lines. **d**. SPNS2 N-domain contains a patch of
161   polar residues adjacent to the DDM head group. **e**. Schematic for GPCR-based
162   transport assay. Media from cells expressing SPNS2 and SphK1 is collected and
163   applied to reporter cells expressing S1PR3 and the Ca^{2+} biosensor obelin. **f**.
164   Measurement of S1P export activity by SPNS2 mutants (N = 24). Data are presented
165   as mean ± SEM.

167   As expected for an MFS transporter, SPNS2 is composed of 12 transmembrane
168   helices organized into pseudo symmetric N- (ND) and C-domains (CD) of TM1-6 and
169   TM7-12 (Supplementary Fig. 4a, b). Notably, TM11 is broken by a well-resolved pi
170   helix (Supplementary Fig. 4c), with a similar feature seen only in structures of the
171   orphan HnSPNS and SLCO6C1 proteins [27,30]. An intracellular helix (ICH1) is found N-
172   terminal of TM7, and a second intracellular helix (ICH2) is located immediately after
173   TM12. Nanobody D12 engages with the cytoplasmic face of the C-domain of SPNS2,
174   with most contacts involving ICH2 and additional interactions with loops L8-9 and L10-

175 11. Notably, the single-particle cryo-EM analysis did not show evidence of structural

176 heterogeneity, suggesting NbD12 stabilizes the inward-facing conformation.

177

178 The transporter adopts a classic inward-facing MFS conformation, with the central

179 binding site open to the cytoplasm (Fig. 1e), similar to the substrate and inhibitor-

180 bound SPNS2 structures (RMSD = 0.51-0.58 Å). The extracellular gate is sealed by

181 opposing pairs of hydrophobic residues on TM1 and TM7, with Tyr246 making a

182 hydrogen bond with the carbonyl of Gly333 (Fig. 1f). This tyrosine-carbonyl hydrogen

183 bond appears conserved among Spinster family transporters, with the equivalent of

184 Tyr246 and Gly333 conserved as tyrosine and alanine or glycine respectively

185 (Supplementary Fig. 2). Beyond this hydrophobic layer, a network of polar residues

186 from TM1b, TM2, TM7, and TM11b form hydrogen bonds and salt bridges which

187 further stabilize the closed extracellular gate.

188

189 **Structure of inward-facing DDM-bound SPNS2**

190 Within the SPNS2 Coulombic potential map, there is an unexpected density within the

191 transporter that is unexplained by the protein model (Fig. 2a). This molecule appears

192 amphipathic, extending from the central cavity into a hydrophobic pocket within the C-

193 domain of SPNS2. While S1P co-purified with SPNS2 after digitonin extraction [28],

194 native mass spectrometry of the DDM-purified SPNS2 did not identify co-purifying S1P

195 [31]. As DDM and sphingosine-1-phosphate are amphipathic molecules with a single

196 acyl chain, we hypothesize the detergent acts as a substrate surrogate and occupies

197 the native substrate's binding site. Supporting this hypothesis, the unknown density

198 fits the acyl chain and first glucose of n-dodecyl-β-D-maltopyranoside. Therefore, we

199 modeled this density as a dodecyl glucoside molecule (Fig. 2b), though we cannot

200 exclude a mixture of DDM and S1P.

201

202 Examining this inward-facing DDM-bound (C_i-DDM) structure of SPNS2, we noted the

203 n-dodecyl-β-D-maltopyranoside primarily contacts the C-domain, with its acyl tail

204 partially inserted into a pocket between TM7, TM8, and TM10 (Fig. 2b, c). This pocket

205 is lined by Thr329, Leu332, Gly333, Ile336, Thr370, Ile411, Ile429, Glu433, Leu436,

206 and Phe437, which are generally conserved in homologs (Supplementary Fig. 4d),

207 supporting this structural motif's importance to binding the hydrophobic tail of S1P.

208 Outside the pocket, the DDM's acyl chain makes further van der Waals contacts with

209 TM1, TM5b, and TM10. Finally, the resolvable glucose moiety of the detergent makes

210 a hydrogen bond with the conserved Trp440 of TM10 (Fig. 2c).

211

Critical motifs to S1P export

212

213 Examining n-dodecyl-β-D-maltopyranoside's engagement with SPNS2, we noted that

214 the detergent's head group interacts with the conventional MFS central cavity and is

215 near a patch of conserved, polar residues on the N-domain (Fig. 2d, Supplementary

216 Fig. 4e-g). Hypothesizing the DDM is acting as a sphingosine-1-phosphate surrogate,

217 the conserved Arg119 of TM1b and His468 of TM11a adjacent to the detergent

218 headgroup immediately suggested these residues coordinate the S1P's anionic head

219 group. Supporting this notion, equivalent residues in SPNS1 and GlpT are essential

220 to their transport of phosphate-containing substrates [32–34]. In contrast, the published

221 state 1 and state 1* structures of SPNS2 in complex with S1P model the substrate

222 head group interacting with TMs 5, 8, and 10 [28]. While both molecules' tails similarly

223 engage the transporter's pocket, the location of S1P's head group between TM5 and

224 TM8 would interfere with a conventional MFS rocker-switch transport mechanism [29].

225 Therefore, we set out to experimentally probe the importance of several S1P

226 interacting residues within SPNS2 to substrate export.

227

228 To probe each residue's role in the sphingosine-1-phosphate export activity of SPNS2,

229 we first established an *in vitro* transport assay to report the export of substrate by

230 taking advantage of the signaling cascade of the high-affinity S1P receptor (Fig. 2e).

231 Media was collected from CHO cells overexpressing sphingosine kinase 1 (SphK1)

232 and SPNS2, or its mutants, after incubation with 1 µM sphingosine. Exported

233 sphingosine-1-phosphate in the media was then quantified by the luminescence of

234 reporter CHO cells expressing S1PR3 and mitochondrially-targeted obelin. Validating

235 this assay, the SPNS2 mutation R200S shows no S1P transport activity (Fig. 2f),

236 recapitulating the loss-of-function phenotype for the equivalent mutation in the *Danio*

237 *rerio* ortholog [2]. Notably, this R200S mutant exhibits an increase in intracellular

238 localization relative to the plasma membrane (Supplementary Fig. 5a). As Arg200 is

239 on TM4 and makes intra-domain hydrogen bonds with the backbone of TM1's Asp118

240 and Arg119 (Supplementary Fig. 5b), this suggests misfolding of the N-domain likely

241 impedes trafficking to the plasma membrane and thereby blocks the protein's S1P

242 export activity.

243

244 As Gly333 has a dual role in sealing the extracellular gate of the inward-facing state

245 and the acyl-chain binding pocket, we hypothesized that mutating this highly

246 conserved side chain would dramatically affect protein localization and activity.

247 Supporting this hypothesis, the glycine-to-leucine mutation G333L reduces plasma

248 membrane localization and sphingosine-1-phosphate export (Fig. 2f, Supplementary

249 Fig. 5a). Curiously, changing the same position to phenylalanine in the mutant G333F

250 further reduces plasma membrane localization while retaining partial transport activity.

251 Nevertheless, the effect of mutating Gly333 on S1P export confirms the importance of

252 this residue to SPNS2's transport cycle.

253

254 Next, we tested the importance of hydrophilic side chains within SPNS2's central

255 cavity and likely near the substrate's head group. Both Tyr116 and Thr322 are highly

256 conserved (Supplementary Fig. 2), and we expected these may hydrogen bond to

257 S1P's phosphate, amine, or hydroxyl moieties. However, mutations to either position

258 did not affect substrate export (Fig. 2f). This indicates both positions are individually

259 dispensable for sphingosine-1-phosphate export, potentially by compensatory

260 interactions of other residues within the central cavity of SPNS2. However, Y116F

261 decreased plasma membrane localization while T322V increased protein on this

262 membrane (Supplementary Fig. 5a), indicating these mutations may affect protein

263 localization or folding.

264

265 **Substrate interactions with SPNS2**

266 As our mutagenesis experiments revealed that several highly conserved residues

267 were dispensable for SPNS2's transport activity, we next applied atomistic molecular

268 dynamics simulations to unambiguously resolve the transporter's interactions with

269 sphingosine-1-phosphate and FTY720-P. Using the SPNS2-DDM structure's

270   detergent as a guide for placing substrate, we performed five 250 ns simulations
271   starting with the substrate in the binding site.

272

273   In most simulations of SPNS2 with sphingosine-1-phosphate, the substrate is stably
274   bound with its head group in the central cavity and the acyl chain within the C-domain's
275   binding pocket (Supplementary Fig. 6a). Normalizing the frequency of contacts
276   between substrate and transporter, we noted the acyl chain of S1P primarily interacts
277   with the pocket lining helices of TM7, TM9, and TM10 (Supplementary Fig. 6b).
278   Further, by clustering all snapshots of the substrate during the simulations, we
279   identified there were several major modes of substrate engagement by the transporter
280   (Fig. 3a, Supplementary Fig. 6c, d). The most populous cluster has the head group
281   engaging exclusively with the C-domain's Trp440 and Asp472 via polar interactions
282   (Fig. 3a). In contrast, in the second and third most populous clusters the substrate
283   makes bridging interactions between domains, connecting Arg119 and sometimes
284   Tyr116 on the ND with His468 and Asp472 on the CD (Supplementary Fig. 6d). This
285   supports the importance of the conserved polar patch of the N-domain to the
286   transporter's substrate-triggered conformational change. Further, the mobility of the
287   head group within the central cavity demonstrates multiple modes of SPNS2-head
288   group interaction. This may explain the lack of an effect for the Y116F mutant on
289   SPNS2 activity, as the nearby Arg119 can compensate in coordinating the S1P's
290   phosphate moiety.

291

292   We next carried out the same simulation strategy with FTY720-P to probe how SPNS2
293   binds this unnatural substrate. As expected, interactions of SPNS2 with the acyl chains
294   S1P and FTY720-P were similar for both substrates (Supplementary Fig. 7b).
295   However, the amine and hydroxyl moieties of FTY270-P interact less frequently with
296   the C-domain relative to sphingosine-1-phosphate. Instead, these groups interact
297   more often with the N-domain's polar patch residues Tyr116, Arg119, and Ile238.
298   Further, we noted in the most populous clusters of simulations that polar moieties of
299   the FTY720-P head group extensively interacted with the N-domain (Fig. 3b,
300   Supplementary Fig. 7b, d), with fewer polar interactions to the C-domain relative to
301   S1P. This appears to be a consequence of the bulky aromatic ring in FTY720-P

302   sterically preventing these hydrogen bonds, though the unnatural substrate has
303   several additional van der Waals contacts between its aromatic ring and the CD.
304   Therefore, we propose hydrophobic interactions of FTY720-P with the C-domain
305   substitute for the polar interactions by S1P to achieve similar substrate-transporter
306   interaction energetics.
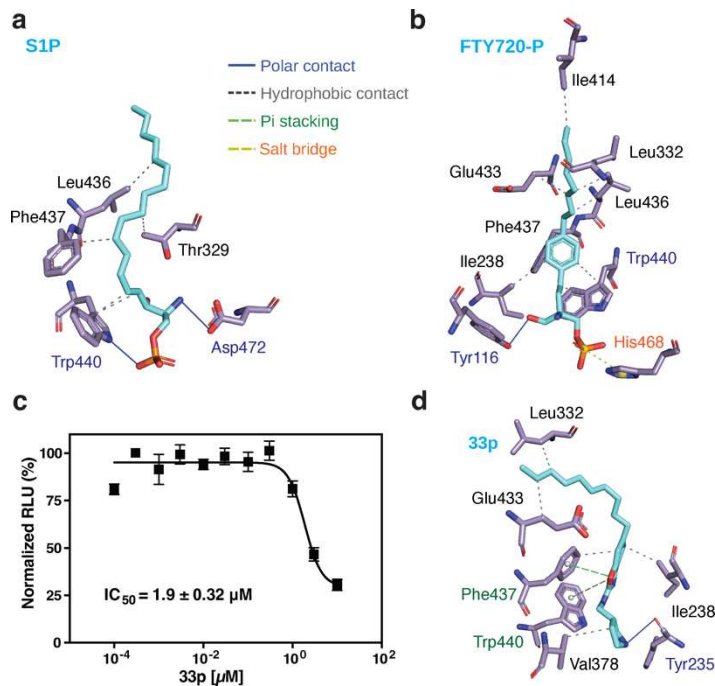
308   **Figure 3. Substrate and inhibitor binding by SPNS2. a**. Sphingosine-1-phosphate
309   head group interactions with SPNS2 in simulation cluster 1. Carbons of SPNS2 side
310   chains and FTY720-P are shown in purple and cyan, respectively. Interaction types
311   are annotated by PLIP [35]. **b**. FTY720-P interactions with SPNS2 in simulation cluster
312   1. **c**. Inhibition of S1P export by 33p measured by S1PR3-coupled export assay (N =
313   8). Data are presented as mean ± SEM. **d**. 33p interactions within SPNS2 in simulation
314   cluster 1.

316   From these results of S1P and FTY720-P binding to SPNS2, we hypothesize the
317   domain-bridging interactions of the substrates' phosphates pull together the ND and
318   CD and thereby trigger the inward-facing to outward-facing conformational switch.
319   This is analogous to the proposed transport of phosphate and glycerol-3-phosphate
320   by GlpT [36].

322   **SPNS2 interactions with inhibitors**
323   Building from these simulations of SPNS2 with substrates, we next sought to describe
324   how the transporter is inhibited by the high-affinity inhibitor 33p [20]. Applying it to the

325 media of the SPNS2-expressing cells, we found the inhibitor had an IC_{50} of 1.9 ± 0.32

326 µM in our S1PR3-coupled S1P export assay (Fig. 3c). As expected, the control

327 compound, SphK1 inhibitor PF543 [37], also inhibited S1P export with an IC_{50} of 232 ±

328 55 nM (Supplementary Fig. 5c), while neither molecule significantly affected S1PR3

329 activity (Supplementary Fig. 5d). This inhibition of S1P export by 33p is 10-fold less

330 potent than previously measured in HeLa cells by LC-MS/MS [20], and may reflect

331 differences in the cell lines or experimental conditions used.

332

333 Examining the transporters' binding to the inhibitor 33p using atomistic molecular

334 dynamics simulations, we observed the inhibitor bound stably with its acyl chain

335 inserted deeply into the C-domain pocket (Supplementary Fig. 8a). This is in contrast

336 to the mobility of the low-affinity inhibitor 16d in a previous molecular dynamics run

337 with SPNS2 [28], and we hypothesize the shallow modeling of this inhibitor into the

338 transporter's CD pocket may affect its stability through the simulation. Clustering the

339 33p simulation snapshots revealed a skewed distribution (Supplementary Fig. 8c),

340 indicating that SPNS2 bound to the molecule is biased to fewer conformations than

341 when bound to substrates. In the two most populous clusters, the secondary amines

342 of 33p's head group make a hydrogen bond with the backbone carbonyl of Tyr116

343 (Fig. 3d, Supplementary Fig. 8d). Supporting the importance of this hydrogen bond to

344 Tyr116, moving or removing the terminal hydrogen bond donors in analogs of 16d and

345 33p dramatically weakened their ability to inhibit SPNS2 [19,20].

346

347 Looking across all simulation snapshots, though also present in cluster 1, we noted

348 33p significantly more frequently makes polar contacts to TM10 in the CD

349 (Supplementary Fig. 8b) while making relatively fewer contacts with TM1. This

350 immediately suggests a competitive inhibition mechanism for 33p, where the molecule

351 binds with high affinity but cannot trigger a complete transport cycle. The numerous

352 interactions of 33p with the CD suggest the molecule binds SPNS2 with high affinity.

353 However, 33p's relatively few and rare interactions with TM1 of the N-domain are

354 insufficient to trigger the transporter's inward-facing to outward-facing conformational

355 change. Consequently, binding to 33p likely arrests SPNS2 in an inward-facing

356 inhibitor-bound state.

357

Apo structure of the transporter

To complement our substrate-bound structure of SPNS2, we next sought to determine the unseen inward-facing apo structure of SPNS2 and thereby describe the protein's conformational change. Examining the SPNS2-DDM structure, we hypothesize the C-domain's narrow acyl-chain binding pocket would sterically exclude larger detergents and therefore purified the protein in the larger diacyl detergent LMNG. NbD12-bound SPNS2 was monodisperse in LMNG (Supplementary Fig. 9a, b), and we determined the complex's structure in this detergent to a resolution of 3.7 Å by cryo-EM (Supplementary Fig. 9c, d).

367
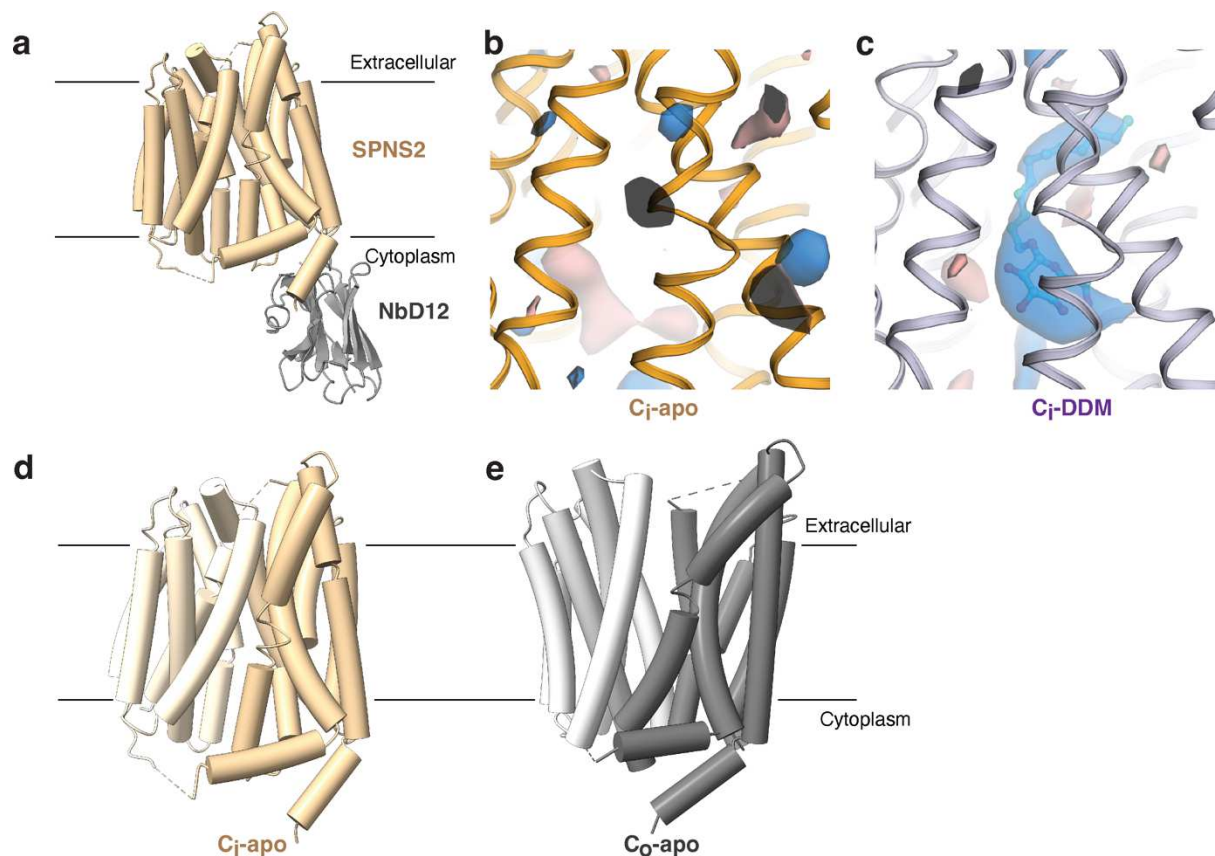
Figure 4. Inward-facing apo structure of SPNS2. a. Structure of the SPNS2-NbD12 complex determined in LMNG, viewed from the plane of the membrane. Difference weighted F_o-F_c density maps near the DDM binding site for the SPNS2-NbD12 complex cryo-EM maps determined in (**b**) LMNG and (**c**) DDM. Maps are contoured at equivalent levels using difference density from omitted sidechains to scale the difference maps. SPNS2 in (**d**) inward-facing and (**e**) outward-facing apo states (PDB: 8EX5).

376

377   Building and refining the SPNS2-NbD12 structure in LMNG (Fig. 4a), the proteins are

378   generally unchanged from the DDM condition (all-atom RMSD = 0.47 Å). Notably,

379   however, there is no apparent non-protein density in the central cavity or pocket of the

380   SPNS2 map determined in LMNG. Further, difference maps calculated using the

381   protein-only SPNS2-NbD12 model gave a large positive density for the structure

382   determined in DDM but not LMNG (Fig. 4b, c). This supports our assignment of the

383   ambiguous density in the SPNS2-DDM map as n-dodecyl-β-D-maltopyranoside and

384   indicates our LMNG map has captured the transporter's inward-facing apo (C_i-apo)

385   state.

386

387   The most pronounced structural change in SPNS2 between apo and DDM-bound

388   states is a ~90° rotation in Trp440, with its side chain rotating roughly parallel to the

389   plane of the membrane in the absence of a head group for hydrogen bonding

390   (Supplementary Fig. 10a). Further, in the presence of DDM, the side chain of Glu433

391   rotates to accommodate the acyl chain and thereby forms a hydrogen bond with

392   Thr373 (Supplementary Fig. 10b). The remaining residues of the substrate binding

393   site do not significantly move, suggesting the substrate binding site is largely pre-

394   formed for efficient binding of amphipathic substrates (Supplementary Fig. 10c).

395

396   **Conformational change of apo SPNS2**

397   Comparing our inward-facing apo SPNS2 and the published outward-facing apo

398   structures, the transporter has undergone a rigid body conformational change

399   consistent with the classic MFS rocker-switch mechanism (Fig. 4d, e). In keeping with

400   this mechanism, the individual N-terminal and C-domains are relatively unchanged

401   between conformations, with all-atom RMSDs of 0.74 Å and 0.62 Å, respectively.

402   However, the relative orientation of the domains has significantly changed due to an

403   inter-domain rotation of 32°. Notably, no significant changes are observed at the

404   NbD12 binding sites or at the termini where MBP and DARPin were fused in the

405   previously published SPNS2$_{cryo}$ construct [28]. This structural consistency suggests the

406   distinct methods of adding fiducial markers for particle alignment during cryo-EM

407   reconstruction did not disturb the transporter's structure.

408

409   While SPNS2's rigid-body inter-domain movement accounts for most of the change

410   between outward- and inward-facing conformations, we noted modest structural

411   differences within the individual domains. The movement from C_o-apo to C_i-apo brings

412   TM2 into greater contact with TM11, inducing an additional half-turn of alpha-helical

413   structure in the previous pi-helix (Supplementary Fig. 10d). This movement of TM2

414   also makes room for the movement of ICH1 toward the transport domain, with the

415   angle between ICH1 and TM7 decreasing by 12° during the C_o-apo to C_i-apo transition

416   (Supplementary Fig 10e). Relative to an idealized MFS rigid body movement, these

417   conformation-specific structural changes likely bias the energetics of SPNS2's

418   outward-facing to inward-facing states.

419

420   **Mechanism of pathogenic SPNS2 mutation in deafness**

421   With our structures of SPNS2 and a model for its S1P transport mechanism, we next

422   sought to understand the pathogenic mechanism for four clinical mutations in SPNS2

423   that cause hearing loss (Fig. 5a) [12,13]. Of these, the nonsense W302* mutation

424   introduces a premature termination at the start of ICH1. Similarly, the frameshift

425   mutation P356fs, located in the loop between TM7 and TM8, leads to mistranslation

426   and subsequent premature stop codon. Ultimately, these incomplete proteins lack

427   significant portions of the C-domain and, therefore, are likely incapable of transport,

428   and accordingly both mutations had insignificant or dramatically reduced S1P export

429   (Fig. 5d).

430

431   In contrast to the pathogenic effects of premature truncations, the pathogenic SPNS2

432   mutations ΔS319 and D163N are associated with hearing loss yet produce full-length

433   or near-full-length proteins. Examining its location within the transporter's structure,

434   we noted Ser319 lies on TM7 and within a conserved set of hydrophilic residues

435   packed between that helix and TM11a (Fig. 5b). We hypothesize that deletion of this

436   residue causes a register shift of that helix, which would result in aberrant packing of

437   TM7 within the C-domain. Supporting this hypothesis, the ΔS319 failed to traffic to the

438   plasma membrane when transiently transfected into HEK cells (Fig. 5g) and resulted

439   in the loss of activity for the mutant (Fig. 5d).

440
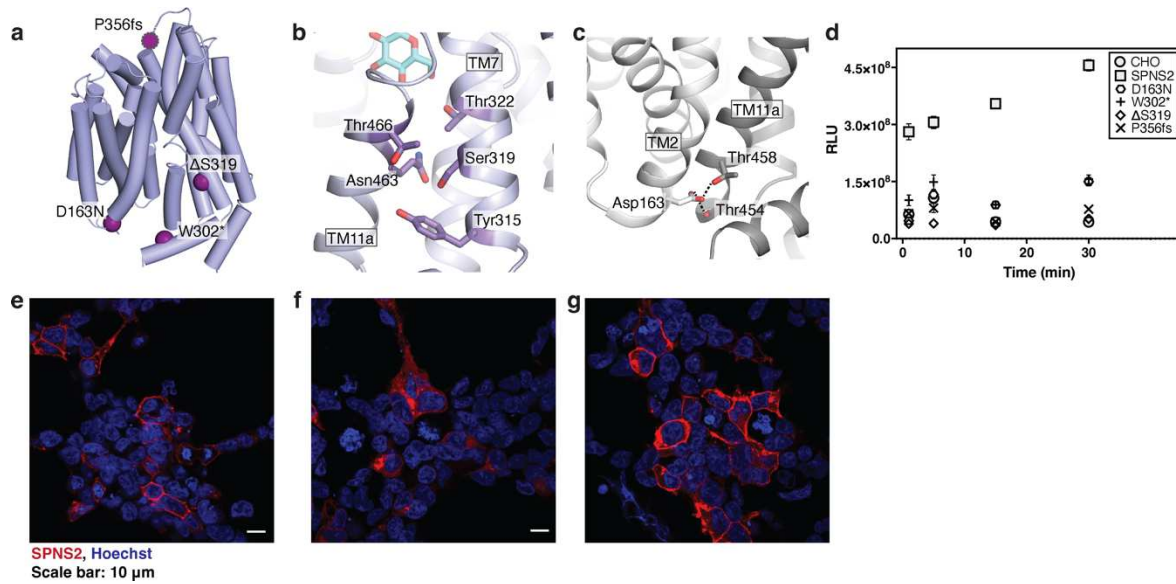
Figure 5. Pathogenic mutations at essential locations in the SPNS2 structures. **a**. Locations of pathogenic SPNS2 mutations within the structure. Loop 7-8 is not resolved in the structure, and the approximate location of Pro356 is indicated by a magenta sphere with a dotted edge. **b**. The pathogenic mutation ΔS319 within the C-domain. **c**. Asp163 in SPNS2 is within the conserved MFS motif A and forms hydrogen bonds specific to the outward-facing conformation. Hydrogen bonds are shown as dotted lines. d. S1P export activity by pathogenic SPNS2 mutants (N = 24). Data are presented as mean ± SEM. Anti-HA immunofluorescence for HEK293-JI cells transiently transfected with HA-tagged SPNS2 (**e**) wild-type or mutants (**f**) ΔS319 and (**g**) D163N.

A third mechanism appears to cause the loss in activity of the pathogenic SPNS2 mutant D163N, as it is on the surface of the N-domain and, therefore, unlikely to affect protein translation or folding (Fig. 5a). Notably, Asp163 is within the conserved motif A of MFS transporters implicated in transporter gating [38]. Accordingly, we noted that while the side chain points toward the cytoplasm in our inward-facing state structures, it interacts with a bend in TM11 of SPNS2's outward-open and outward-occluded states (Fig. 5c). Here, it hydrogen bonds with the side chain of Thr458 and the backbone carbonyl of Thr454. Therefore, we expect the D163N mutation to weaken these interactions, disturbing the energetics of SPNS2's transport cycle without significantly affecting protein folding. Supporting this hypothesis, the D163N mutant of SPNS2 correctly traffics to the plasma membrane (Fig. 5g) and has partial S1P export activity (Fig. 5d). This modest activity of the D163N mutant suggests there is a minimal S1P export activity needed from SPNS2 for proper development of the stria vascularis, below which it becomes disorganized and thereby leads to hearing loss.

467

Discussion

In this study, we identify the biophysical mechanisms of SPNS2's interactions with sphingosine-1-phosphate, the immunomodulator FTY720-P, and the targeted inhibitor 33p through a combination of structural studies, *in vitro* binding, *in vivo* transport, and molecular dynamics simulations. These results provide a framework for understanding the transporter's mechanism for substrate export, and inhibition of this process by small molecules. Further, by capturing an inward-facing apo state, we identify modest changes in the transporter's secondary structure which affect the outward-to-inward conformational change. Finally, coupling our structural results and protein localization, our results explain the pathogenic effects of SPNS2 mutations implicated in hearing loss.

Notably, our analysis of SPNS2 binding to substrates S1P and FTY720-P provides new insights into the transporter's action on those molecules. In our simulations, we did not observe S1P or FTY720-P binding between TM5 and TM8, as was modeled previously for S1P [28]. It remains unclear if the previously modeled S1P location is an intermediate step of the reaction cycle, an artifact of the substrate interacting with the saposin nanodisc, or a modeling error due to poor local resolution. Nevertheless, our updated location for substrate binding supports SPNS2 using a classic MFS rocker-switch transport mechanism. Further, our structural and MD analysis identified conserved residues within the N-domain's polar patch that are likely critical to triggering the conformational change, supported by the failure of the inhibitor 33p to engage these side chains. This makes clear that engaging both domains is central to triggering the transport cycle, and is highly analogous to the phosphate bridging seen in GlpT [36].

These structures also hint at a role for SPNS2's Glu433, which is unusual for being a charged residue conserved within the acyl-chain binding pocket and the hydrophobic core of the C-domain. Examining all available structures, we noted this side chain is highly mobile within the pocket in the absence of S1P or analogs and potentially interacts with solvent or Thr370 (Supplementary Fig. 10b). However, upon loading of

499 substrates, it consistently makes a hydrogen bond with Thr373. This same Thr373-
500 Glu433 hydrogen bond is also found in the outward-occluded apo state structures of
501 SPNS2 [28]. Therefore, it is tempting to hypothesize the orientation and hydrogen
502 bonding of Glu433 is acting as a switch to enable the transporter's conformational
503 change which triggered by the substrate's acyl chain, or stochastically in the apo state.
504 How the state of this glutamate is propagated to affect more significant structural
505 changes in the protein is unclear. However, we suspect in an extended conformation
506 it could hydrogen bond more frequently or strongly with Thr370 and nearby waters,
507 thereby altering the outward-facing state's energetic stability.

508

509 Notably, in our molecular dynamics study, one simulation each for sphingosine-1-
510 phosphate and FTY270-P showed the substrate leaving the binding site and moving
511 closer to the cytoplasmic surface of the protein (Supplementary Fig. 6a, 7a). These
512 transits of substrate away from the binding site are too rare for statistical analysis.
513 Nevertheless, the S1P and FTY720-P travel we observed align with the orientation of
514 these molecules in the inner membrane after synthesis inside the cell, and hint at a
515 path for substrate movement to and from the transporter's binding site.

516

517 Finally, while SPNS2's essential role in the pharmacokinetics of fingolimod by
518 exporting FTY720-P is well known, our structural and biochemical results suggest the
519 transporter may play a role in the metabolism and movement of other therapeutic small
520 molecules. Our DDM-bound structure indicates SPNS2 is relatively promiscuous for
521 amphiphilic molecules with a single acyl chain. Therefore, SPNS2 may play a role in
522 the pharmacokinetics of other analogs of sphingosine-1-phosphate which target the
523 S1P receptors, and other pharmacophores with a single acyl chain.

524

Methods

Sequence alignment

SPNS2 orthologs, MFS-fold lipid transporters, and prototype MFS transporters were aligned in Promals3D [39] and rendered with ESPript [40].

Cloning, expression, and purification of SPNS2

The full-length human SPNS2 gene was cloned into the pHTBV1.1 plasmid containing a C-terminal tobacco etch virus (TEV) protease cleavage site followed by EGFP, twin-Strep, and 10×His affinity tags. Baculovirus was then generated according to the previously described protocols [31,41,42].

The resulting baculovirus was used to infect Expi293F cells in Freestyle 293 expression medium (GIBCO) in the presence of 5 mM sodium butyrate. Infected cells were grown in an orbital shaker for 72 h at 37 °C, 8% CO_2 and 75% humidity, harvested by centrifugation, washed with phosphate-buffered saline, flash-frozen, and stored at -80 °C until further use.

The cell pellets were resuspended in extraction buffer (300 mM NaCl, 50 mM HEPES pH 7.5, 1% DDM or 1% LMNG) in the presence of cOmplete Protease Inhibitor Cocktail tablets (Roche) and solubilized at 4 °C for 1 h with gentle rotation. The insoluble materials were pelleted at 50,000 × g for 40 min. The supernatants were incubated with pre-equilibrated TALON resin (Takara) and allowed to bind for 1 h at 4 °C. The resin was poured onto a gravity-flow column and washed with column buffer (300 mM NaCl, 50 mM HEPES pH 7.5, and 0.03% DDM (Anatrace) or 0.01% LMNG (Anatrace)) supplemented with 10 mM $MgCl_2$, 1 mM ATP, and 10 mM imidazole. Protein was eluted with elution buffer (300 mM NaCl, 50 mM HEPES pH 7.5, 300 mM imidazole and 0.03% DDM). The eluate was incubated with pre-equilibrated Strep-Tactin XT Superflow resin (IBA-Lifesciences) for 1 h at 4 °C. The resin was poured onto a gravity-flow column and washed with column buffer. Protein was eluted with column buffer supplemented with 50 mM D-biotin, followed by tag-cleavage with TEV protease overnight and reverse IMAC purification using TALON resin.

557   The tag-cleaved SPNS2 proteins were concentrated using a centrifugal concentrator

558   with 100 kDa cut off (Sartorius) and subjected to size exclusion chromatography using

559   a Superdex 200 10/300 GL column (GE Healthcare) pre-equilibrated with gel filtration

560   buffer (150 mM NaCl, 20 mM HEPES pH 7.5, 0.025% DDM or 0.002% LMNG). Peak

561   fractions were pooled and concentrated for subsequent experiments.

562

563   **Cloning, expression, and purification of biotinylated SPNS2**

564   Full-length codon-optimized SPNS2 with a C-terminal AVI and Flag tag and BirA were

565   cloned into in-house Baculovirus expression vector pD-INS3, and baculovirus

566   produced using standard methods [41,42]. For protein expression, Sf9 cells at 4×10^6

567   cells/mL were co-infected with SPNS2 and BirA virus with MOI 1 and 0.3, respectively,

568   and cultured at 27 °C with biotin supplemented in the medium. Cells were harvested

569   by centrifugation after 72 h, and cell pellets solubilized in 50mM HEPES pH7.5,

570   300mM NaCl,10% glycerol supplemented with protease inhibitor, benzonase, 2 mM

571   biotin and 1% DDM or 1% LMNG. After solubilization at 4°C for 1.5 h, insoluble

572   material was removed by ultracentrifugation at 35,000 × g for 1 h. Supernatant was

573   incubated with Anti-Flag M2 resin (Sigma) for 1.5 h at 4 °C. The resin was washed

574   with 30 column volumes of 50 mM HEPES pH 7.5, 300 mM NaCl, 5% glycerol with

575   0.026% DDM or 0.01% LMNG. The protein was eluted with 50 mM HEPES pH 7.5,

576   300 mM NaCl, 5% glycerol, 200µg/ml Flag-peptide with 0.026% DDM or 0.01% LMNG.

577   Eluted protein fractions were concentrated using a 100 kDa Amicon Ultra centrifugal

578   filter (Millipore) and applied to a Superose 6 increase 10/30 GL (GE) gel filtration

579   chromatography column pre-equilibrated in 20 mM HEPES pH 7.5, 150 mM NaCl with

580   0.026% DDM or 0.003% LMNG. SEC fractions were analyzed by SDS-PAGE and

581   pooled accordingly. Purified SPNS2 was supplemented with 10% glycerol, aliquoted,

582   flash frozen and stored at -80°C until use.

583

584   **Cloning, expression, and purification of VNUP**

585   Full-length VNUP was cloned into in-house mammalian expression vector pD-MAM8.1

586   with a C-terminal AVI and Flag tag. For protein expression, Expi293F cells at 1×10^6

587   cells/mL were transiently transfected with 1mg/L DNA/PEI complex with DNA:PEI ratio

588   of 1:3. Cells were incubated at 37 °C, 8% CO_2 for 72 h post-transfection and harvested

589 by centrifugation. Cell pellets were solubilized in 50 mM Tris-HCl pH 7.5, 200 mM

590 NaCl, 20 mM KCl, 30% glycerol supplement with protease inhibitor, benzoase and 1%

591 LMNG (Anatrace). After solubilization at 4 °C for 1.5 h, insoluble material was removed

592 by ultracentrifugation at 35,000 × g for 1 h. Supernatant was incubated with Anti-Flag

593 M2 resin (Sigma) for 1.5 h at 4 °C. The resin was washed with 20 column volumes of

594 50 mM Tris-HCl pH 7.5, 100 mM NaCl, 10 mM KCl, 1 mM ATP, 10 mM MgCl$_2$, 20%

595 glycerol, 0.01% LMNG, followed by a second wash step with 50 mM Tris-HCl pH 7.5,

596 100 mM NaCl, 10 mM KCl, 20 % glycerol, 0.01 % LMNG. The protein was eluted with

597 50 mM Tris-HCl pH 7.5, 100 mM NaCl, 10 mM KCl, 20 % Glycerol, 0.01 % LMNG, and

598 200 µg/ml Flag-Peptide. Eluted protein fractions were concentrated using a 50-kDa

599 molecular-weight (MW) cut-off Amicon Ultra centrifugal filter (Millipore), and further

600 purified using size exclusion chromatography on a Superose 6 Increase 10/30 GL in

601 50mM Tris-HCl pH 7.5, 100 mM NaCl, 10 mM KCl, 10% Glycerol, 0.01% LMNG. Peak

602 fractions were analyzed by SDS-PAGE and pooled accordingly. Purified VNUP was

603 aliquoted, flash frozen, and stored at -80 °C until use.

604

605 **Thermal stability assay of SPNS2 and VNUP**

606 The thermal stability assay was performed with nanoDSF assay. SPNS2 or VNUP at

607 1 µM concentration were incubated with 0-160 µM of FTY720-P (stock concentration

608 1.6mM in DMSO) in 20 mM HEPES pH 7.5, 150 mM NaCl, 10% DMSO with 0.026%

609 DDM or 0.003 % LMNG. All samples were incubated for 30 min at room temperature

610 prior to analysis. After incubation, samples were loaded into high sensitivity grade

611 nanoDSF capillaries (Nanotemper), measured in Prometheus NT.48 device

612 (Nanotemper) with excitation power 100% and temperature gradient from 20 °C to 90

613 °C with a slope of 2 °C/min. Data were analyzed using PR ThermControl software

614 (Nanotemper).

615

616 **Nanobody generation**

617 To induce the development of heavy chain-only antibodies (IgG2 and IgG3) in alpacas,

618 animals were immunized four times at 2-week intervals, each time with 150-200 µg of

619 purified protein. All the procedures concerning alpaca immunization were approved by

620 the Cantonal Veterinary Office of Zurich, Switzerland (License No. ZH 198/17). SPNS2

621   was delivered in proteoliposomes consisting of soy asolectin, porcine brain polar lipid

622   extract, cholesterol, and monophosphoryl hexa-acyl lipid A (Avanti Polar Lipids) at a

623   ratio of 24:8:7:0.5 by weight in PBS. Before injections, antigens were mixed in a 1:1

624   (vol/vol) ratio with GERBU Fama adjuvant (GERBU Biotechnik GmbH, Heidelberg,

625   Germany) and injected subcutaneously in 100 μL aliquots into the shoulder and neck

626   region. Two weeks after the last boost, 80 mL of blood was collected from the jugular

627   vein for isolation of lymphocytes (Ficoll-Paque PLUS, GE Healthcare Life Sciences,

628   and Leucosep tubes, Greiner). Approximately 50 million cells were used to isolate

629   mRNA (RNeasy Mini Kit, Qiagen) that was then reverse transcribed into cDNA

630   (AffinityScript, Agilent, USA) using the VH gene-specific primer. The V_HH (nanobody)

631   repertoire was amplified by two PCRs and phage library was generated using

632   established methods [43], fragment exchange cloning into a SapI-linearized pDX

633   phagemid vector using 336 ng of the V_HH repertoire and 1 μg of the plasmid DNA.

634

635   The resulting nanobody library (size 2×10^8) was screened by biopanning against

636   indirectly immobilized targets. For this purpose, biotinylated SPNS2 in 20 mM HEPES

637   pH 7.5, 150 mM NaCl with 0.015% DDM and 0.0015% CHS was immobilized (1 μg

638   SPNS2 per well) on Streptavidin or Neutravidin-coated microplates (alternating

639   between selection rounds) at 5 μg/mL, 100 μL per well in 96 well Maxisorp plate (Nunc,

640   Denmark) and two rounds of selections were performed until ~1000-fold positive

641   enrichment of phages was obtained. Single clones for 190 nanobodies were

642   expressed as polyhistidine-tagged soluble nanobodies in the bacterial periplasm and

643   analyzed by ELISA for binding to SPNS2.

644

645   Ninety-six ELISA-positive clones were Sanger sequenced and a phylogenetic analysis

646   with the resulting binder sequences for each target was performed using MMseqs2 [44].

647   Sequences were clustered based on a minimum sequence identity of 85% and

648   representative sequences were chosen from 9 clusters. Selected binder sequences

649   were subcloned into a pBXNP plasmid (Addgene #110098) that was modified to

650   contain 1x FLAG tag upstream of the 10x His tag. Binders were finally purified from

651   the periplasm of MC1061 bacteria according to the published protocol [45].

652

Surface Plasmon Resonance assay of SPNS2

The binding affinities of Nanobody D12 and F09 were determined using Biacore 8K machine (Cytiva). Biotinylated SPNS2 protein was immobilized on the SA sensor chip to a target level of 600 to 800 RU. Purified nanobodies were serial diluted with running buffer (20 mM HEPES pH 7.5, 150 mM NaCl, 0.026% DDM, 0.01% fatty acid free BSA) to a concentration gradient between 0 to 1 or 10 µM. The diluted nanobody series were injected over the immobilized sensor in running buffer at 25 °C while binding traces monitored simultaneously. Data fitting was analyzed with 1:1 interaction model using the Biacore Insight Evaluation software (Cytiva).

Cell lines and culture conditions

The Jump In T-REx human embryonic kidney 293 cell line (HEK293-JI) expressing doxycycline-inducible human SPNS2 were generated by RESOLUTE as described previously [46]. Briefly, codon-optimized sequences of wild type and mutant SPNS2 in pDONR221 (Addgene #132307) were subcloned into a modified pJTI R4 DEST CMV TO pA plasmid (Thermo Fisher Scientific) containing Twin-Strep-Tag (IBA Lifesciences) and HA epitopes (SH tag) at the N or the C terminus of SPNS2 as indicated. All constructs were confirmed by Sanger sequencing. HEK293-JI cells stably expressing each construct were selected in DMEM medium (Sigma-Aldrich, D5796) supplemented with 10% FBS and 5% Pen/Strep (Sigma-Aldrich, P4333), 0,0005% Blasticidin (Invivogen, ant-bl-05) and 4% Geneticin (Sigma-Aldrich, A1720) for one week. After selection, cells were kept in DMEM medium supplemented with 10% FBS and 5% Pen/Strep and protein expression was induced for 24 h with 10 µg/mL doxycycline (Sigma-Aldrich, D9891).

Immunofluorescence

To detect localization of SPNS2 in HEK293-JI-SPNS2-SH cells, the cells were seeded at a density of 1.2×10^5 on glass microscopic cover slips coated with Poly-L-lysine (Sigma P2658) already placed into 24-well plates (Corning). 16 h after protein induction with 1 µg/mL doxycycline, cells were fixed and permeabilized in 4% PFA for

684   15 min at RT. Cells were subsequently incubated in blocking buffer containing 10%

685   FCS and 0.3% Triton X-100 in 1x PBS for 1 h at room temperature. Next, samples

686   were incubated with anti-HA from rat (Roche, 60789700, 1:1000) antibody for 2 h at

687   room temperature. After three washing steps, cells were incubated with secondary

688   antibodies anti-rat coupled to Alexa Fluor 488 (Thermo Fisher Scientific, A-11006,

689   1:500) and DAPI (Sigma, D9542, 10mM) diluted 1:1000 for 1 h at room temperature.

690   After three washing steps (two times blocking buffer, one-time 1x PBS), the slides we

691   mounted with ProLong medium diamond (Invitrogen) and stored at 4 °C. Imaging was

692   performed using confocal microscope LSM980 (Zeiss) with 63x objective and obtained

693   images were processed in Zen blue 3.3 software (Zeiss).

694

695   To detect co-localization of NbD12 and NbF09 with SPNS2 and localization of SPNS2

696   transport mutants (using NbF09) the protocol above was used with following the

697   adaptations: after fixation and blocking, the cells were firstly incubated with NbD12 or

698   NbF09 for 2 h at room temperature in presence of 0.3% TRITON-X 100. After three

699   washing steps, samples were incubated simultaneously with anti-HA from rabbit (Cell

700   Signaling Technology, C29F4, 1:400) and anti-FLAG-M2 from mouse (Sigma, F3165

701   ,1:1000) antibodies for 2 h at room temperature. After three washing steps, cells were

702   simultaneously incubated with secondary antibodies goat anti-rabbit coupled to Alexa

703   Fluor 594 (Thermo Fisher Scientific, A-11012, 1:500), goat anti-mouse coupled to

704   Alexa Fluor 488 (Thermo Fisher Scientific, A-11001, 1:500) and DAPI (Sigma D9542

705   10mM) diluted 1:1000 for 1 h at room temperature.

706

707   To detect localization of SPNS2 hearing loss mutants, the HEK293-JI cells were

708   transiently transfected with respective plasmids using L-PEI and SPNS2 expression

709   was induced with 1 μg/mL doxycycline 24 h after transfection. The protocol above was

710   performed with the following adaptations: after fixation and blocking, the cells were

711   incubated with anti-HA from rabbit (Cell Signaling Technology, C29F4, 1:400) and

712   simultaneously incubated with secondary antibodies goat anti-rabbit coupled to Alexa

713   Fluor 594 (Thermo Fisher Scientific, A-11012, 1:500) and DAPI (Sigma D9542 10mM)

714   diluted 1:1000 for 1 h at room temperature.

715

Cell lysis, co-immunoprecipitation, and western blotting

Approximately 10×10^6 cells were lysed in 250 µL of lysis buffer composed of 50 mM HEPES pH 7.4, 250 mM NaCl, 5 mM EDTA, and 1% NP-40, supplemented with Roche EDTA-free protease inhibitor cocktail (1 tablet per 50 mL) and incubated for 30 min on ice. Lysates were cleared by centrifugation at 13,000 rpm, 15 min, 4 °C and total protein concentration was quantified using a Bradford protein assay (Bio-Rad). Samples were diluted to 0.5 mg of total protein per sample. Subsequently, 200 µL clarified and diluted lysate was mixed with 1 µg nanobody and incubated at 4 °C overnight. Immunoprecipitation was carried out using equilibrated anti-FLAG M2 affinity gel (Sigma, #A2220) for 2 h at 4 °C, with beads collected by centrifugation at 13,000 rpm, 15 min, 4 °C and subsequently washed three times with 1x TBS buffer. The bound protein fraction was eluted with 0.1 M glycine-HCl. For western blot analysis, 1 µL of input and 3 µL of each eluted sample were run on 10% SDS-polyacrylamide gel in Tris-Glycine running buffer and transferred to nitrocellulose membranes Amersham Protran 0.45 mm (GE Healthcare). The membranes were blocked with 5% non-fat dry milk in TBST and probed with primary antibodies anti-HA from rabbit (Cell Signaling Technology, C29F4, 1:2000) and anti-FLAG-M2 from mouse (Sigma, F3165, 1:2000) at 4 °C overnight followed by secondary antibodies goat anti-mouse HRP (115-035-003, Jackson ImmunoResearch) and goat anti-rabbit HRP (111-035-003, Jackson ImmunoResearch). Binding was detected with horseradish-peroxidase-conjugated secondary antibodies using the ECL western blotting system (Thermo Fisher Scientific).

Cryo-EM sample preparation and data collection

For purification of the SPNS2-NbD12 complex, SPNS2 after reverse IMAC purification and SEC purified NbD12 were mixed at 1:1.5 molar ratio, incubated at 4 °C for 1 h, and the complex purified by size exclusion chromatography using a Superdex 200 10/300 GL column (GE Healthcare) pre-equilibrated with gel filtration buffer (150 mM NaCl, 20 mM HEPES pH 7.5, 0.025% DDM or 0.002% LMNG).

Cryo-EM grids of SPNS2-NbD12 were prepared on freshly glow discharged QuantiFoil Au R1.2/1.3 300-mesh grids (Quantifoil) using a Mark IV Vitrobot (Thermo Fisher

748   Scientific) at 100% humidity and 4 °C, and then plunged into liquid ethane. Peak

749   fractions of SPNS2-NbD12 in DDM were pooled, concentrated to 14 mg/mL, and

750   plunge-frozen on the QuantiFoil grid after blotting for 5.0 s. Peak fractions of SPNS2-

751   NbD12 in LMNG were similarly pooled and concentrated to 6 mg/mL, then plunge-

752   frozen on the QuantiFoil grid after blotting for 8.0s.

753

754   The SPNS2-NbD12 in DDM dataset was collected on a Titan Krios electron

755   microscope, using a GIF-Quantum energy filter with a 20 eV slit width (Gatan) and a

756   K3 direct electron detector (Gatan) at a dose rate of 17.5 e$^-$/px/sec. EPU (Thermo

757   Fisher Scientific) was used to automatically record three movie stacks per hole in

758   super-resolution mode with 2x binning with the defocus ranging from −1.0 to −2.4 μm.

759   Each micrograph was dose-fractioned into 40 frames, with an accumulated dose of

760   40.74 e$^-$/Å^2.

761

762   The SPNS2-NbD12 in LMNG dataset was collected on a Titan Krios electron

763   microscope, using a GIF-Quantum energy filter with a 20eV slit width (Gatan) and a

764   K3 direct electron detector (Gatan). EPU (Thermo Fisher Scientific) was used to

765   automatically record two movie stacks per hole in super-resolution mode with 2x

766   binning, at a dose rate of 14.3 e$^-$/px/sec with the defocus ranging from −1.0 to −2.4

767   μm. Each micrograph was dose-fractioned into 40 frames, with an accumulated dose

768   of 41.42 e$^-$/Å^2.

769

770   **Reconstruction of SPNS2-NbD12**

771   cryoSPARC was used for both data processing workflows [47]. Movies were patch

772   motion corrected and CTF-corrected and manually curated based on ice thickness

773   and CTF fit resolution.

774

775   For the DDM dataset, particles were blob-picked, followed by two cycles of 2D

776   classification. The particles from well-resolved 2D classes were used for template-

777   based picking and the resultant particles were then subjected to 2D classification, *ab*

778   *initio* models generation and preliminary heterogeneous classifications. Particles from

779   a good class of heterogeneous refinement were used for Topaz [48] training and picking.

780   Topaz and template-picked particles were then combined, duplicates removed, and
781   polished by two cycles of 2D classification. Iterative *ab initio* models generation and
782   heterogeneous classifications further polished particles at 3D stage. Non-uniform
783   refinement yielded a reconstruction for the SPNS2-NbD12 complex at 3.68 Å. To
784   improve the map, local refinement was performed with the mask applied to exclude
785   the DDM micelle and yielded a final map at a nominal resolution of 3.68 Å.

786

787   For the LMNG dataset, particles were blob picked, followed by three cycles of 2D
788   classification. The particles from well-resolved 2D classes were used for template-
789   based picking followed by further 2D and 3D classification. Particles from the best
790   resolved class of heterogeneous refinement were then used for Topaz training and
791   picking. Topaz and template-picked particles were then combined, and duplicates
792   removed. Iterative ab initio models generation and heterogeneous classifications
793   further polished particles at 3D stage. Non-uniform refinement yielded reconstructions
794   for the SPNS2-NbD12 complex at 3.98 Å. Local refinement was performed with the
795   protein-only mask applied and yielded a map at 3.69 Å.

796

797   **Model building and refinement**
798   Models were initially built using the DDM dataset. The human SPNS2 protein model
799   from AlphaFold [49] and the nanobody protein model from published structures of PCFT
800   [50] were roughly fitted into the experimental map and used as templates for model
801   building in Coot [51]. Following manual adjustments, models were refined with
802   phenix.real_space_refine using default geometric restraints [52]. For the LMNG dataset,
803   the SPNS2-NbD12 model in DDM was used as template in Coot. Only the acyl chain
804   and first glucose unit of the DDM headgroup were well resolved in the SPNS2-DDM
805   cryo-EM map and have been included in the model. Residual density for the second
806   glucose unit is present at lower contour level but is somewhat disconnected from the
807   rest of the molecule and was not included in the final model. Secondary structure
808   within the models was identified by DSSP [53]. Model-to-map FSCs and validation
809   statistics are listed in Supplementary Table 1.

810

811　Weighted F_o-F_c difference maps were calculated following refinement of the protein

812　model alone using ServalCat in the CCPEM software package [54]. Difference maps for

813　the DDM and LMNG datasets were scaled by calculating reference maps for models

814　in which tyrosine sidechains near the bound detergent were omitted.

815

816　**S1PR3-coupled transport assay**

817　Generation and cloning of Spns2 wild type and mutant sequences into the piggyBac

818　vector was performed by DNA-Cloning-Service e.K. (Hamburg, Germany). SphK1 and

819　SPNS2 wild type or mutant overexpressing cells were generated by transfection of

820　CHO-K1 cells using GeneJET according to manufacturer´s specification (Roche

821　Diagnostics GmbH, Mannheim, Germany). Stably transfected clone pools were

822　obtained by selection with 0.25 mg/mL Zeocin (InvivoGen, San Diego, CA, USA). CHO

823　cells stably overexpressing S1PR3 and mitochondrially-targeted obelin were

824　generated in-house (Bayer AG, Wuppertal, Germany). All cell lines were cultured in

825　PAN medium (PAN Biotech, Aldersbach, Germany) containing 10% dialyzed FCS and

826　kept under sterile conditions at 37 °C and 5% CO_2.

827

828　All luminescent measurements of the activation assay were performed on 384-well

829　microtiter plates (MTPs) using a FLIPR Penta High-Throughput Cellular Screening

830　System (Molecular Devices, San Jose, CA, USA). Therefore, 5000 cells/well of

831　SPNS2 wild type and mutant transfected cells were seeded in 25 µL Optimem

832　containing 1% dialyzed FCS. For S1PR3 transfected cells, 5000 cells/well were

833　seeded in 20 µL Optimem containing 1% dialyzed FCS with 5 µg/mL coelenterazine.

834　Cells were incubated for 24 h at 30 °C and 5% CO_2. Sphingosine (Sigma-Aldrich,

835　Munich, Germany) dilution was prepared in Tyrode (130 mM NaCl, 5 mM KCl, 20 mM

836　HEPES, 1 mM $MgCl_2$, 2 mM $CaCl_2$, 4.8 mM $NaHCO_3$ at pH 7.4) containing 0.3% BSA

837　and added to the SPNS2 wild type and mutant cells with a final concentration of 1 µM.

838　Cells were incubated for 1, 5, 15 or 30 min at 37 °C and 5% CO_2. In the following step,

839　20 µL supernatant from SPNS2 wild type and mutant cells was transferred to the

840　S1PR3 cells within the FLIPR device and luminescence signals, expressed as relative

841　light units (RLUs), were measured for 60 sec.

842

843   To evaluate the effects of the SPNS2 inhibitor 33p (SLB1122168) and the PF543

844   SPNS2 wild type and S1PR3 overexpressing cells were seeded as described. A

845   dilution series of 33p (Probechem Biochemicals Co Ltd, Shanghai, China) and PF543

846   (Sigma-Aldrich, Munich, Germany) was performed in DMSO and Tyrode containing

847   1:500 SmartBlock (Candor Bioscience GmbH, Wangen, Germany) was added. The

848   dilution series, starting at 10 µM, was then transferred to the SPNS2 cells and

849   incubated for 10 min at room temperature. Subsequently, sphingosine with a final

850   concentration of 1 µM was added to the SPNS2 cells and incubated for a further 15

851   min at 37 °C and 5% CO_2. Supernatant of the SPNS2 cells was then transferred to the

852   S1PR3 cells within the FLIPR device and luminescence signals were measured for 60

853   sec. The effect of 33p and PF543 on the S1PR3 was quantified by adding the

854   compounds' dilution series, starting at 10 µM, onto the S1PR3 overexpressing cells

855   and incubating for 10 min at room temperature. Subsequently, the luminescence

856   signals were measured for 60 sec in the FLIPR device.

857

858   **Molecular dynamics simulations**

859

860   The coordinates of the inward-facing conformation of SPNS2 were obtained from its

861   DDM-bound cryo-EM structure. All missing residues of SPNS2 and its residues with

862   unresolved sidechains were modelled using Modeller 9 [55]. The topologies for all

863   substrates i.e. S1P, FTY720-P, and 33P, were parametrised using the CHARMM-GUI

864   ligand reader and modeler [56] and the CHARMM36 general forcefield [57]. The phosphate

865   headgroups of S1P and FTY720-P substrates were modelled based on their

866   protonation states in solution [58] since they are highly likely to interact with solvent when

867   bound to SPNS2 in its inward-facing conformation. All substrates were then docked

868   into the SPNS2 central cavity using Autodock Vina [59] and the pose best mimicking the

869   DDM-bound pose were considered for simulations.

870

871   The CHARMM-GUI web-server [60] was used to set up all atomistic molecular dynamics

872   simulations. During the setup, SPNS2 was inserted into a model membrane containing

873   a total of 251 POPC lipids and 13 PI(4,5)P_2 lipids. The outer leaflet of the membrane

874   contained only POPC lipids whereas the inner leaflet contained a 90:10 ratio of

875   POPC:PI(4,5)P_2 lipids. The solvent in all simulations comprised of the TIP3P water

876   model [61] along with 0.15 M of Na$^+$ and Cl$^-$ ions, and an addition number of Na$^+$ ions to

877   neutralize the net charge of the entire system. All simulations used the CHARMM36m

878   force field [62] and were performed using the GROMACS 2020.3 simulation suite [63].

879   Following the standard CHARMM-GUI protocol for membrane protein systems, our

880   simulation systems were first relaxed by performing energy minimization using the

881   steepest descent algorithm followed by several steps of equilibration during which

882   positional restraints on the protein were gradually released. The equilibration stage

883   was not considered for analyses. During equilibration, the Berendsen barostat [64] was

884   used whereas other parameter settings were maintained during production

885   simulations and explained below. At the end of the equilibration phase for each of the

886   three substrate-containing systems, the model membranes containing the protein and

887   substrate measured 10 nm^2 along the membrane plane and 11.71 ± 0.19 nm along

888   the perpendicular axis. These final snapshots of the equilibration phase were used to

889   generate initial snapshots with five different initial velocities for production simulations

890   for each substrate. Each of these five production simulations were conducted for 250

891   ns each with 2 fs timestep. This was performed for each substrate bound to SPNS2.

892   The V-rescale thermostat [65] maintained the temperature at 310 K and the Parrinello-

893   Rahman semi-isotropic barostat [66] maintained the pressure at 1 bar throughout all

894   production simulations with a compressibility of 4.5x10^{-5}/bar. The LINCS algorithm [67]

895   was used to apply constraints on all bond lengths. The cutoffs for Coulombic and van

896   der Waals interaction radii were set to 1.2 nm. Van der Waals interactions were treated

897   with a cutoff algorithm alongside a Force-switch modifier while long-range electrostatic

898   interactions were treated by the Particle Mesh Ewald algorithm [68]. Every frame in each

899   production simulation was generated at 100 ps intervals.

900

901   The clustering analyses of the conformations of each substrate within the SPNS2

902   cavity was performed using the in-built '*gmx cluster*' tool of GROMACS. All five

903   simulations were concatenated and frames at regular intervals of 1 ns were used.

904   During clustering, the Gromos method was used along with a RMSD cutoff of 0.1 nm.

905   The coordinates of the protein-substrate complex obtained from each of the top three

906   populous clusters were uploaded to the Protein-Ligand Interaction Profiler (PLIP) web-

907   server [69], which then provided annotated data on different forms of protein-substrate

908   interactions along with PyMOL-compatible visualization states. PyMOL

909   (https://pymol.org/2/) and Visual Molecular Dynamics (VMD) [70] were used for

910 visualization. Xmgrace (https://plasma-gate.weizmann.ac.il/Grace/) was used for
911 plotting.
912

References

913

1. Liu, Y. *et al.* Edg-1, the G protein–coupled receptor for sphingosine-1-phosphate, is essential for vascular maturation. *J. Clin. Invest.* **106**, 951–961 (2000).

2. Kawahara, A. *et al.* The Sphingolipid Transporter Spns2 Functions in Migration of Zebrafish Myocardial Precursors. *Science* **323**, 524–527 (2009).

3. Wang, Z. *et al.* Mfsd2a and Spns2 are essential for sphingosine-1-phosphate transport in the formation and maintenance of the blood-brain barrier. *Sci. Adv.* **6**, eaay8627 (2020).

4. Schwab, S. R. *et al.* Lymphocyte Sequestration Through S1P Lyase Inhibition and Disruption of S1P Gradients. *Science* **309**, 1735–1739 (2005).

5. Pérez-Jeldres, T., Alvarez-Lobos, M. & Rivera-Nieves, J. Targeting Sphingosine-1-Phosphate Signaling in Immune-Mediated Diseases: Beyond Multiple Sclerosis. *Drugs* **81**, 985–1002 (2021).

6. McGinley, M. P. & Cohen, J. A. Sphingosine 1-phosphate receptor modulators in multiple sclerosis and other conditions. *The Lancet* **398**, 1184–1194 (2021).

7. Pyne, N. J. & Pyne, S. Sphingosine 1-phosphate and cancer. *Nat Rev Cancer* **10**, 489–503 (2010).

8. Spiegel, S. & Milstien, S. Functions of the multifaceted family of sphingosine kinases and some close relatives. *J Biol Chem* **282**, 2125–2129 (2007).

9. Nishi, T., Kobayashi, N., Hisano, Y., Kawahara, A. & Yamaguchi, A. Molecular and physiological functions of sphingosine 1-phosphate transporters. *Biochimica et Biophysica Acta (BBA) - Molecular and Cell Biology of Lipids* **1841**, 759–765 (2014).

936 10. Mendoza, A. *et al.* The Transporter Spns2 Is Required for Secretion of Lymph

937   but Not Plasma Sphingosine-1-Phosphate. *Cell Reports* **2**, 1104–1110 (2012).

938 11. Kichaev, G. *et al.* Leveraging Polygenic Functional Enrichment to Improve

939   GWAS Power. *The American Journal of Human Genetics* **104**, 65–75 (2019).

940 12. Mardani, S., Almadani, N. & Garshasbi, M. Compound heterozygous variants in

941   SPNS2 cause sensorineural hearing loss. *European Journal of Medical Genetics*

942   **66**, 104658 (2023).

943 13. Ingham, N. J. *et al.* Mouse screen reveals multiple new genes underlying mouse

944   and human hearing loss. *PLoS Biol* **17**, e3000194 (2019).

945 14. Hisano, Y., Kobayashi, N., Kawahara, A., Yamaguchi, A. & Nishi, T. The

946   Sphingosine 1-Phosphate Transporter, SPNS2, Functions as a Transporter of

947   the Phosphorylated Form of the Immunomodulating Agent FTY720. *Journal of*

948   *Biological Chemistry* **286**, 1758–1766 (2011).

949 15. Matloubian, M. *et al.* Lymphocyte egress from thymus and peripheral lymphoid

950   organs is dependent on S1P receptor 1. *Nature* **427**, 355–360 (2004).

951 16. Brinkmann, V. *et al.* The Immune Modulator FTY720 Targets Sphingosine 1-

952   Phosphate Receptors. *Journal of Biological Chemistry* **277**, 21453–21457 (2002).

953 17. Camm, J., Hla, T., Bakshi, R. & Brinkmann, V. Cardiac and vascular effects of

954   fingolimod: Mechanistic basis and clinical implications. *American Heart Journal*

955   **168**, 632–644 (2014).

956 18. Cartier, A. & Hla, T. Sphingosine 1-phosphate: Lipid signaling in pathology and

957   therapy. *Science* **366**, eaar5551 (2019).

958 19. Fritzemeier, R. *et al.* Discovery of In Vivo Active Sphingosine-1-phosphate

959   Transporter (Spns2) Inhibitors. *J. Med. Chem.* **65**, 7656–7681 (2022).

960 20. Burgio, A. L. *et al.* 2-Aminobenzoxazole Derivatives as Potent Inhibitors of the

961   Sphingosine-1-Phosphate Transporter Spinster Homolog 2 (Spns2). *J. Med.*

962   *Chem.* **66**, 5873–5891 (2023).

963 21. Lambert, E., Mehdipour, A. R., Schmidt, A., Hummer, G. & Perez, C. Evidence

964   for a trap-and-flip mechanism in a proton-dependent lipid transporter. *Nat*

965   *Commun* **13**, 1022 (2022).

966 22. Harvat, E. M. *et al.* Lysophospholipid Flipping across the Escherichia coli Inner

967   Membrane Catalyzed by a Transporter (LplT) Belonging to the Major Facilitator

968   Superfamily. *Journal of Biological Chemistry* **280**, 12028–12034 (2005).

969 23. Nguyen, C. *et al.* Lipid flipping in the omega-3 fatty-acid transporter. *Nat*

970   *Commun* **14**, 2571 (2023).

971 24. Wood, C. A. P. *et al.* Structure and mechanism of blood–brain-barrier lipid

972   transporter MFSD2A. *Nature* **596**, 444–448 (2021).

973 25. Cater, R. J. *et al.* Structural basis of omega-3 fatty acid transport across the

974   blood–brain barrier. *Nature* **595**, 315–319 (2021).

975 26. Martinez-Molledo, M., Nji, E. & Reyes, N. Structural insights into the

976   lysophospholipid brain uptake mechanism and its inhibition by syncytin-2. *Nat*

977   *Struct Mol Biol* **29**, 604–612 (2022).

978 27. Zhou, F. *et al.* Crystal structure of a bacterial homolog to human lysosomal

979   transporter, spinster. *Science Bulletin* **64**, 1310–1317 (2019).

980 28. Chen, H. *et al.* Structural and functional insights into Spns2-mediated transport of

981   sphingosine-1-phosphate. *Cell* S0092867423004579 (2023)

982   doi:10.1016/j.cell.2023.04.028.

983   29. Huang, Y., Lemieux, M. J., Song, J., Auer, M. & Wang, D.-N. Structure and

984   Mechanism of the Glycerol-3-Phosphate Transporter from *Escherichia coli*.

985   *Science* **301**, 616–620 (2003).

986   30. Lin, S., Ke, M., Zhang, Y., Yan, Z. & Wu, J. Structure of a mammalian sperm

987   cation channel complex. *Nature* **595**, 746–750 (2021).

988   31. Tang, H. *et al.* The solute carrier SPNS2 recruits PI(4,5)P2 to synergistically

989   regulate transport of sphingosine-1-phosphate. *Molecular Cell*

990   S1097276523005099 (2023) doi:10.1016/j.molcel.2023.06.033.

991   32. He, M. *et al.* Spns1 is a lysophospholipid transporter mediating lysosomal

992   phospholipid salvage. *Proc. Natl. Acad. Sci. U.S.A.* **119**, e2210353119 (2022).

993   33. Law, C. J., Enkavi, G., Wang, D.-N. & Tajkhorshid, E. Structural Basis of

994   Substrate Selectivity in the Glycerol-3-Phosphate: Phosphate Antiporter GlpT.

995   *Biophysical Journal* **97**, 1346–1353 (2009).

996   34. Law, C. J. *et al.* Salt-bridge Dynamics Control Substrate-induced Conformational

997   Change in the Membrane Transporter GlpT. *Journal of Molecular Biology* **378**,

998   828–839 (2008).

999   35. Adasme, M. F. *et al.* PLIP 2021: expanding the scope of the protein–ligand

1000   interaction profiler to DNA and RNA. *Nucleic Acids Research* **49**, W530–W534

1001   (2021).

1002 36. Lemieux, M. J., Huang, Y. & Wang, D.-N. The structural basis of substrate

1003   translocation by the Escherichia coli glycerol-3-phosphate transporter: a member

1004   of the major facilitator superfamily. *Current Opinion in Structural Biology* **14**, 405–

1005   412 (2004).

1006   37. Schnute, M. E. *et al.* Modulation of cellular S1P levels with a novel, potent and

1007   specific inhibitor of sphingosine kinase-1. *Biochemical Journal* **444**, 79–88

1008   (2012).

1009   38. Jiang, D. *et al.* Structure of the YajR transporter suggests a transport mechanism

1010   based on the conserved motif A. *Proc. Natl. Acad. Sci. U.S.A.* **110**, 14664–14669

1011   (2013).

1012   39. Pei, J., Kim, B.-H. & Grishin, N. V. PROMALS3D: a tool for multiple protein

1013   sequence and structure alignments. *Nucleic Acids Research* **36**, 2295–2300

1014   (2008).

1015   40. Robert, X. & Gouet, P. Deciphering key features in protein structures with the

1016   new ENDscript server. *Nucleic Acids Research* **42**, W320–W324 (2014).

1017   41. Raturi, S. *et al.* High-Throughput Expression and Purification of Human Solute

1018   Carriers for Structural and Biochemical Studies. *JoVE* 65878 (2023)

1019   doi:10.3791/65878.

1020   42. Mahajan, P. *et al.* Expression Screening of Human Integral Membrane Proteins

1021   Using BacMam. in *Structural Genomics* (eds. Chen, Y. W. & Yiu, C.-P. B.) vol.

1022   2199 95–115 (Springer US, 2021).

1023   43. Geertsma, E. R. & Dutzler, R. A Versatile and Efficient High-Throughput Cloning

1024   Tool for Structural Biology. *Biochemistry* **50**, 3272–3278 (2011).

1025   44. Steinegger, M. & Söding, J. MMseqs2 enables sensitive protein sequence

1026   searching for the analysis of massive data sets. *Nat Biotechnol* **35**, 1026–1028

1027   (2017).

1028   45. Zimmermann, I. *et al.* Generation of synthetic nanobodies against delicate

1029   proteins. *Nat Protoc* **15**, 1707–1741 (2020).

1030   46. Polesel, M. *et al.* Functional characterization of SLC39 family members ZIP5 and

1031   ZIP10 in overexpressing HEK293 cells reveals selective copper transport activity.

1032   *Biometals* **36**, 227–237 (2023).

1033   47. Punjani, A., Rubinstein, J. L., Fleet, D. J. & Brubaker, M. A. cryoSPARC:

1034   algorithms for rapid unsupervised cryo-EM structure determination. *Nat Methods*

1035   **14**, 290–296 (2017).

1036   48. Bepler, T. *et al.* Positive-unlabeled convolutional neural networks for particle

1037   picking in cryo-electron micrographs. *Nat Methods* **16**, 1153–1160 (2019).

1038   49. Jumper, J. *et al.* Highly accurate protein structure prediction with AlphaFold.

1039   *Nature* **596**, 583–589 (2021).

1040   50. Parker, J. L. *et al.* Structural basis of antifolate recognition and transport by

1041   PCFT. *Nature* **595**, 130–134 (2021).

1042   51. Emsley, P. & Cowtan, K. *Coot*: model-building tools for molecular graphics. *Acta*

1043   *Crystallogr D Biol Crystallogr* **60**, 2126–2132 (2004).

1044   52. Afonine, P. V. *et al.* Real-space refinement in *PHENIX* for cryo-EM and

1045   crystallography. *Acta Crystallogr D Struct Biol* **74**, 531–544 (2018).

1046   53. Kabsch, W. & Sander, C. Dictionary of protein secondary structure: Pattern

1047   recognition of hydrogen-bonded and geometrical features. *Biopolymers* **22**,

1048   2577–2637 (1983).

1049   54. Yamashita, K., Palmer, C. M., Burnley, T. & Murshudov, G. N. Cryo-EM single-

1050   particle structure refinement and map calculation using Servalcat. *Acta*

1051   *Crystallogr D Struct Biol* **77**, 1282–1291 (2021).

1052   55. Webb, B. & Sali, A. Protein Structure Modeling with MODELLER. in *Protein*

1053   *Structure Prediction* (ed. Kihara, D.) vol. 1137 1–15 (Springer New York, 2014).

1054 56. Kim, S. *et al.* CHARMM-GUI ligand reader and modeler for CHARMM force field

1055   generation of small molecules: CHARMM-GUI Ligand Reader and Modeler for

1056   CHARMM Force Field Generation of Small Molecules. *J. Comput. Chem.* **38**,

1057   1879–1886 (2017).

1058 57. Vanommeslaeghe, K. *et al.* CHARMM general force field: A force field for drug-

1059   like molecules compatible with the CHARMM all-atom additive biological force

1060   fields. *J Comput Chem* **31**, 671–690 (2010).

1061 58. Naor, M. M., Walker, M. D., Van Brocklyn, J. R., Tigyi, G. & Parrill, A. L.

1062   Sphingosine 1-phosphate pKa and binding constants: Intramolecular and

1063   intermolecular influences. *Journal of Molecular Graphics and Modelling* **26**, 519–

1064   528 (2007).

1065 59. Trott, O. & Olson, A. J. AutoDock Vina: Improving the speed and accuracy of

1066   docking with a new scoring function, efficient optimization, and multithreading. *J*

1067   *Comput Chem* **31**, 455–461 (2010).

1068 60. Jo, S., Kim, T., Iyer, V. G. & Im, W. CHARMM-GUI: A web-based graphical user

1069   interface for CHARMM. *J Comput Chem* **29**, 1859–1865 (2008).

1070 61. Mark, P. & Nilsson, L. Structure and Dynamics of the TIP3P, SPC, and SPC/E

1071   Water Models at 298 K. *J. Phys. Chem. A* **105**, 9954–9960 (2001).

1072 62. Huang, J. *et al.* CHARMM36m: an improved force field for folded and intrinsically

1073   disordered proteins. *Nat Methods* **14**, 71–73 (2017).

1074 63. Abraham, M. J. *et al.* GROMACS: High performance molecular simulations

1075   through multi-level parallelism from laptops to supercomputers. *SoftwareX* **1–2**,

1076   19–25 (2015).

1077   64. Berendsen, H. J. C., Postma, J. P. M., Van Gunsteren, W. F., DiNola, A. & Haak,

1078   J. R. Molecular dynamics with coupling to an external bath. *The Journal of*

1079   *Chemical Physics* **81**, 3684–3690 (1984).

1080   65. Bussi, G., Donadio, D. & Parrinello, M. Canonical sampling through velocity

1081   rescaling. *The Journal of Chemical Physics* **126**, 014101 (2007).

1082   66. Parrinello, M. & Rahman, A. Polymorphic transitions in single crystals: A new

1083   molecular dynamics method. *Journal of Applied Physics* **52**, 7182–7190 (1981).

1084   67. Hess, B., Bekker, H., Berendsen, H. J. C. & Fraaije, J. G. E. M. LINCS: A linear

1085   constraint solver for molecular simulations. *J. Comput. Chem.* **18**, 1463–1472

1086   (1997).

1087   68. Darden, T., York, D. & Pedersen, L. Particle mesh Ewald: An $N \cdot \log(N)$ method

1088   for Ewald sums in large systems. *The Journal of Chemical Physics* **98**, 10089–

1089   10092 (1993).

1090   69. Salentin, S., Schreiber, S., Haupt, V. J., Adasme, M. F. & Schroeder, M. PLIP:

1091   fully automated protein–ligand interaction profiler. *Nucleic Acids Res* **43**, W443–

1092   W447 (2015).

1093   70. Humphrey, W., Dalke, A. & Schulten, K. VMD: Visual molecular dynamics.

1094   *Journal of Molecular Graphics* **14**, 33–38 (1996).

1095

1096

1097

1098

1099

1100

Ethic statement

The immunizations of alpaca were conducted strictly according to the guidelines of the Swiss Animals Protection Law and were approved by the Cantonal Veterinary Office of Zurich, Switzerland (Licenses No. ZH 198/17 and ZH028/2021).

1133

Author contributions

1134 **Author contributions**

1135 H.Z.L., Y.N.C., C.M., A.S., G.M., S.M. cloned, expressed, and purified SPNS2. S.S.

1136 immunized the alpaca, generated the nanobody library, and identified positive binders.

1137 H.Z.L., Y.N.C., and A.S. expressed, purified, and characterized the nanobodies. Z.G.

1138 and G.W. generated knock-out, stably expressing, and transiently transfected cell

1139 lines and performed immunofluorescence experiments. H.Z.L. and A.C.W.P. collected

1140 and processed the cryo-EM images and built atomic models. H.Z.L., A.C.W.P., and

1141 D.B.S. analyzed the structures. J.S., H.C.S., F.W., H.B., and A.P.F. designed and

1142 performed the S1P transport assay. D.P. and S.K. designed and carried out the

1143 molecular dynamics simulations. A.G. and D.B.S. designed, completed, and evaluated

1144 the bioinformatics analysis. H.Z.L., A.C.W.P., and D.B.S. wrote the manuscript. All

1145 authors discussed and edited the manuscript. B.M.K., N.A.B.B., T.W., K.L.D., V.P.,

1146 A.E., S.K., A.I.P., G.S.F., and D.B.S. supervised the research.

1147

1148 **Competing interests**

1149 The authors declare no competing interests.

Supplementary Files

This is a list of supplementary files associated with this preprint. Click to download.

- Supplementarydata15nov2023c300.pdf